HHS Public Access

Author manuscript

J Aerosol Sci. Author manuscript; available in PMC 2017 May 01.

Published in final edited form as:

J Aerosol Sci. 2016 May ; 95: 54–66. doi:10.1016/j.jaerosci.2016.01.004.

Three-dimensional computational fluid dynamics modeling of particle uptake by an occupational air sampler using manually-scaled and adaptive grids

Andrea C. Landázuri[a,b], **A. Eduardo Sáez**[a], and **T. Renée Anthony**[c]

[a]The University of Arizona, Department of Chemical and Environmental Engineering, 1133 E James E. Rogers Way, Tucson, AZ 85641, United States

[b]Universidad San Francisco de Quito USFQ, Colegio de Ciencias e Ingenierías “El Politécnico”, Departamento de Ingeniería Química, Calle Diego de Robles y Vía Interoceánica, Cumbayá, Casilla Postal: 17-1200-841, Quito, Ecuador

[c]The University of Iowa, Department of Occupational and Environmental Health, 145 N. Riverside Drive, S300, Iowa City, IA 52242-5000, United States

Abstract

This work presents fluid flow and particle trajectory simulation studies to determine the aspiration efficiency of a horizontally oriented occupational air sampler using computational fluid dynamics (CFD). Grid adaption and manual scaling of the grids were applied to two sampler prototypes based on a 37-mm cassette. The standard *k*–ε model was used to simulate the turbulent air flow and a second order streamline-upwind discretization scheme was used to stabilize convective terms of the Navier–Stokes equations. Successively scaled grids for each configuration were created manually and by means of grid adaption using the velocity gradient in the main flow direction. Solutions were verified to assess iterative convergence, grid independence and monotonic convergence. Particle aspiration efficiencies determined for both prototype samplers were undistinguishable, indicating that the porous filter does not play a noticeable role in particle aspiration. Results conclude that grid adaption is a powerful tool that allows to refine specific regions that require lots of detail and therefore better resolve flow detail. It was verified that adaptive grids provided a higher number of locations with monotonic convergence than the manual grids and required the least computational effort.

Keywords

Computational fluid dynamics; Occupational sampler; k–ε model; Adaptive grid; Monotonic convergence; Turbulent flow

1. Introduction

Occupational air samplers are used to assess human exposure to potentially toxic particulate matter due to inhalation. Typical samplers used for this purpose operate at flow rates between 2 and 4 L/min. However, research based on the prototypes presented in this work suggests that samplers could operate at suction flow rates as high as 10 L/min, which allows for sampling the same amount of air as with conventional samplers in a shorter period of

time and, from another perspective, allows for reduction of the detection limit of sampled mass over the same period (Anthony & Flynn, 2006).

CFD has been used as a tool to design sampling devices that monitor occupational exposure to aerosols that have the potential to cause respiratory system damage (Li, Lundgren & Rovel-Rixx, 2000). Direct experimental methods require the use of wind tunnels and are considerably more expensive than CFD simulations (Griffiths & Boysan, 1996), and modeling of occupational aerosol samplers using CFD generally has been based on two-dimensional simulations. The few three-dimensional studies usually lack geometric details due to memory or CPU limitations. Usual details that are left out include a realistic simulation of the sampler's inlet and the torso of the person on which the sampler is placed (Bird, 2005).

Convergence of the iterative methods and grid (or mesh) independence studies are of great importance prior to validation of the results obtained by CFD to ensure that comparison of the model with experimental data has genuine value (Tam et al. (2000) and Richmond-Bryant (2003)). Iterative convergence and grid independence analyses are usually done following verification procedures described in previous works (Stern, Wilson, Coleman, & Paterson (2001) and Roache (1998)) where three successively scaled grids are suggested for this purpose. However, it is important to consider that if the original grid is already very refined, the computational resources to generate and store the other two grids may become limited and simulations may take too long to converge to an appropriately low tolerance. On the other hand, if the original grid is too coarse, even two successively scaled grids may not be enough to obtain an accurate solution. Monotonic convergence is checked by calculation of the local mesh convergence ratio, defined by Roache (1998) as:

$$R_2 = \frac{\|e_{mid,fine}\|^2}{\|e_{coarse,mid}\|^2} \quad (1)$$

$$\|e\|^2 = \sqrt{\sum e_{j,k}^2} \quad (2)$$

and $e_{j,k}$ is the difference between the coarser (j) and finer (k) mesh level values for a given degree of freedom. Calculation of R_2 requires finding the numerical solution for three grid sizes (coarse, medium and fine). Mesh convergence is acceptable when local R_2 values are <1 for all degrees of freedom, which, for turbulent flows, include pressure (P), the three components of the time-averaged velocity (U_x, U_y, U_z), the turbulent kinetic energy (k) and the turbulent energy dissipation rate (ε).

In this work, both manual and adaptive grid scaling were used to verify the validity of the simulations. The grid quality of geometries such as the ones presented in this work required especial attention in order to avoid undesirable geometrical properties such as skewness, which can later influence in grid independence. All grids complied with the criterion of having a maximum skewness of less than 0.95 (Fluent, Inc, 2005).

Two 3-D facing-the wind, horizontally-oriented occupational samplers mounted on an elliptical torso, emulating the human body, and placed in a wind tunnel were considered. These samplers consist on a multi-orifice opening and were designed based on two-dimensional numerical studies. A multi-orifice inlet reduces wind effects and equalizes pressure variations inside the sampler, leading to uniformity in the deposition of particles on the filter. The sampler designs are based on the widely used three-piece 37-mm air sampling cassette and include a new sampling head that contains 1043 openings 254-μm in diameter. The prototypes presented in this work operate in conditions typical of indoor work environments at 293 K, 1 atm and a free-stream velocity of 0.4 m/s. One of the prototypes required an additional simulation parameter, which is the permeability of the filter. A more detailed discussion about the decision-making process for the proposed prototypes' design as well as the comparison of the model with respect to humanoid aspiration efficiency can be found elsewhere (Anthony, Landázuri, Van Dyke & Volckens, 2010).

The original grid used in the CFD calculations study contains triangular finite elements on each surface and tetrahedral elements to discretize the 3D domain. The final simulations were carried out using the standard k–ε model. This model shows good convergence and performs well for external flow problems around complex geometries (Fluent, Inc, 2005). Furthermore, based on a comparison of computation times, the standard k–ε model used relatively low memory requirements than the turbulent simulations using the RNG k–ε equations which were also tried, but its results have not been included in this work. The complete model runs with a pressure-based solver, along with the Green–Gauss cell-based discretization method for gradients and derivatives to generate iteratively the air flow field solution from the steady-state, incompressible, turbulent Navier–Stokes equations. Second order upwind schemes provide more accurate solutions than first order schemes, yet, depending on the nature of the problem, first order simulations may work adequately as well based on grid independence analysis (Fluent, Inc, 2005). The Green–Gauss node-based method is also known to provide more accurate solutions than the Green–Gauss cell-based method, but the former requires more computational time. Hence, since accuracy and less computational effort are crucial in this type of investigation, the final simulations were carried under second-order upwind schemes applied directly and using the Green–Gauss cell-based method. Once the fluid flow solution was evaluated, particle trajectory simulations were carried out to estimate the samplers' efficiency for particles with diameter in the range 6–100 μm.

Results from the simulations can be used to: (1) determine the effectiveness of the sampler to: (i) assess human exposure, (ii) improve sampler design and (iii) identify geometrical simplifications for grid generation depending on a specific interest; (2) emphasize the importance of grid convergence and grid independence assessment; and (3) recognize grid adaption as alternate tool to solve mixed flow regime problems.

2. Geometry

2.1. Wind tunnel and elliptical torso

A wind tunnel that extends 1.1 m upstream, 2 m downstream, and +/−0.9 m laterally from the point of reference represents the volume of air that surrounds the sampler and torso. The

human torso is simulated as a simplified truncated cylinder. The study by Anderson & Anthony (2013) determined that the differences in aspiration efficiencies between three torso geometries: (i) a simplified truncated cylinder, (ii) a non-truncated cylinder, and (iii) an anthropometrically realistic humanoid body, were <8.8% over all particle sizes, indicating that there is little difference in aspiration efficiency between torso models. Grid independence and convergence analysis can be applied in the same manner for an improved version that includes more realistic torso geometries.

The origin of coordinates in the 3-D domain is the central pore of the samplers. The floor of this simulated wind tunnel is at the −0.3 m position where the torso truncates, and the top of the tunnel extends 0.6 m above the torso (Fig. 1).

The wind tunnel consists of two volumes that bisect the torso in order to have better control of the grid density surrounding the torso and near the vicinity of the sampler. The blockage ratio of the torso in this wind tunnel is 9.6%, which implies an acceptable torso diameter to lateral wind tunnel dimension, which ensures an accurate description of the flow characteristics (Zdravkovich, 2003, Anagnostopoulos & Iliadis, 1996). Both samplers are positioned to the right (0.38 m) of the centerline of a 0.26 m wide by 0.127 m deep elliptical cylinder representing a human torso. Both sampler prototypes, presented in Fig. 2, have an inlet face that has 1043 pores with 254-μm diameter, and operate at a suction flow rate of 10 L/min. For this study, all models were developed at conditions typical of indoor work environments, with a free-stream air velocity of 0.4 m/s at 293 K.

2.2. Configuration of sampler 1

In addition to the previous features, this sampler consists on a 4-mm exhaust port that operates at the defined flow rate of 10 L/min (Fig. 2a). The inside of the cassette contains a 5-mm pore size filter of mixed cellulose ester (MCE) where aerosols are typically collected. The total thickness of the filter, which includes the thickness of a backup pad, is equal to 9.538×10^{-4} m, and the calculated filter permeability is 1.19×10^{-12} m^2 based on the application of Darcy's Law with velocity and pressure drop laboratory data. Fig. 2d and e shows a prototype of this sampler that was used in wind tunnel experiments.

2.3. Configuration of sampler 2

In general, the more geometric features are added in a model the more computationally expensive the simulation is. In the case of sampler 1, the porous jump provides an extra boundary to be satisfied; therefore more degrees of freedom need to be solved during the simulation. For this reason, in order to aid in convergence, a simpler configuration (sampler 2) was generated where the sampler has the same inlet design and same suction rate as the first one, but the filter and the 4 mm diameter exit are excluded from the model (Fig. 2b).

3. Methods and models

Gambit 2.4.6 (Ansys Inc., Lebanon, NH) was the preprocessor used for geometry and grid generation and Fluent 6.3.26 (Ansys Inc., Lebanon, NH) was the software used to perform flow simulations. All simulations were performed on 64-bit processor PCs with 8 gigabytes RAM using Windows XP.

The 3-D meshed geometry requires special attention to avoid undesirable geometrical properties, such as skewness, that may influence grid independence results. The geometric domain presented in this work, for example, is associated with a Reynolds number of Re=9270, based on diameter of the torso, whereas the pore openings are associated with smaller Reynolds number Re=56. Therefore, it is not only necessary to capture these detailed flow features, but also to verify that the flow field solution is independent of the constructed grids. An incorrect evaluation of the flow field solution can be incurred if the local size of the grids is not considered in greater extent and variations in the smaller portion of the domain, the sampler inlet grid, can affect the whole flow field solution (Dussin, Fossati, Guardone & Vigevano, 2009). The aforementioned drawbacks are particularly encountered when manual scaling of grids is used, since several attempts may be needed to generate a grid that can reach a converged solution from which subsequent scaling will be performed and that can achieve the least computational effort.

3.1. Definition of the appropriate model

During the initial steps of the investigation, several grids representing the sampler 1 configuration were generated to investigate the sensitivity to turbulence models, relaxation parameters and orders of solution. The pressure-based solver along with the Green Gauss node-based and cell based discretization methods for gradients and derivatives were tested to generate iteratively the air flow field solution from the steady-state, incompressible, turbulent Navier–Stokes equations. In order to determine which turbulent model was more suitable time-wise, the RNG, Realizable and Standard k–ε models were tested using first order discretization schemes. It was observed that in the majority of cases, laminar simulations served as indicators of whether the solutions were going to converge or diverge. If the solution converged, the flow field result was used as initial guess for subsequent first order upwind turbulent simulations. It was also observed that on average, the Standard k–ε model takes 15% and 25% less time per iteration than the RNG and Realizable k–ε models, respectively. In addition, changes in relaxation parameters could be avoided completely when using the Standard k–ε model whereas the RNG k–ε model not only required more time to reach convergence, but also more than one change in relaxation parameters had to be made to force the equations to converge. The realizable k–ε model presented more difficulties since solution limits, which keep the solutions within acceptable ranges, had to be increased, increasing as well the risk of flow variables to become zero, negative or excessively large during a calculation (Fluent, Inc, 2005). Under the same premise, first order solutions were also used as initial guesses for second order simulations.

The Green–Gauss node-based method is known to provide more accurate solutions than the Green–Gauss cell-based method; however, during the testing of grids, it was observed that the former required approximately 33% more time.

Final simulations to solve the air flow field used the steady-state, incompressible, turbulent Standard k–ε Navier–Stokes equations with standard wall functions. The governing equations were solved sequentially in Fluent® using the pressure-based segregated algorithm along with the SIMPLE pressure–velocity coupling method. In the models proposed in this work, the Green–Gauss cell-based method for evaluation of gradients and derivatives,

second order upwind schemes for momentum, k and ε equations, and standard scheme for pressure were applied directly. Solutions from these simulations were saved sequentially at global solution errors (*GSE*) equal to 10^{-3}, 10^{-4} and 5×10^{-5} (sampler 1) and 5.5×10^{-5} (sampler 2).

3.2. Fluid flow verification

To evaluate the quality of the flow field solutions, iterative tolerance, grid independence and percentage of locations with monotonic convergence were calculated for six degrees of freedom (P, U_x, U_y, U_z, k and ε) at locations where particle trajectory simulations were to be performed. Information on these degrees of freedom were extracted from 1722 points located upstream of the sampler. The region that contained these points extended from X= −0.1 to −0.75 m, Y=+/−0.2 m and Z =−0.15 to 0.15 m.

Iterative tolerance was assessed using the L_2 error norm,

$$L_2=\frac{\left[\sum (x_i - x_{i-1})^2\right]^{0.5}}{\left[\sum (x_i)^2\right]^{0.5}} \quad (3)$$

where the subscripts refer to level of *GSE* tolerance: *i-1* is the value at the larger *GSE* tolerance limit and summation is over all nodes of the computational area of interest, that is, over the 1722 points upstream the sampler. An L_2 error norm of less than 5% over all degrees of freedom (x) was set as criterion for having an adequately solved grid at a sufficiently low *GSE* tolerance. Grid independence was evaluated using Eq. (1). Monotonic convergence occurs when $0<R_2<1$; the solution is then said to be grid independent; $R_2>1$ represents a divergent solution (Roache, 1998).

3.3. Particle trajectory simulations

Once the flow field solutions were verified, particle trajectory simulations were performed for spherical unit density particles of 6, 12.5, 25, 50, 75, 90 and 100 μm in diameter with no evaporation. The discrete phase model (DPM) chosen used a maximum number of 20,000 steps and a length scale of 5×10^{-5} m. These values were confirmed to be appropriate for this type of study in a previous work (Anthony et al., 2010) and cover all possible length scales of the domain (Bird, 2005). The DPM follows the Euler–Lagrange approach. The fluid phase is treated as a continuum by solving the Navier–Stokes equations, while the dispersed phase is solved by tracking a large number of particles, through the calculated flow field (i.e. air). Fluent® predicts the trajectory of a discrete phase particle by integrating the force balance on the particle, written in a Lagrangian reference frame. This force balance equates particle inertia with the forces acting on the particle and can be written as

$$\frac{dU_p}{dt}=F_D(U-U_p)+\frac{g_x(\rho_p-\rho)}{\rho_p}+F_x \quad (4)$$

Where F_x is an additional acceleration (force/unit particle mass) term, $F_D(U-U^p)FD(U-Up)$ is the drag force per unit particle mass and

$$F_D = \frac{18\mu}{\rho_p d_p^2} \frac{C_D \mathrm{Re}}{24} \quad (5)$$

where, UU is the fluid phase velocity, U_pUp is the particle velocity, μμ is the dynamic viscosity of the fluid, ρρ is the fluid density, ρ_pρp is the density of the particle, $d_p$dp is the particle diameter and C_D is the drag coefficient, defined by Eq. (6) (Anthony et al., 2010) where "a_1, a_2 and a_3 are constants that apply for smooth spherical particles over several ranges of *Re*" given by Morsi and Alexander (1972). *Re* is the relative Reynolds number, which is defined by Eq. (7).

$$C_D = a_1 + \frac{a_2}{\mathrm{Re}} + \frac{a_3}{\mathrm{Re}^2} \quad (6)$$

$$\mathrm{Re} \equiv \frac{\rho d_p |U_p - U|}{\mu} \quad (7)$$

Equation (4) incorporates additional forces (F_xFx) in the particle force balance that can be important under special circumstances. This term may include aerodynamic lift, F_L; Magnus force due to spinning and electrostatic forces, F_E. Lift is perpendicular to the oncoming flow direction, in contrast with the drag force, which is parallel to the flow direction. It has been shown that the lift forces, Magnus force and electrostatic forces are typically two orders of magnitude smaller than the gravitational force and F_D, therefore they are often not considered (Tu, Inthavong, & Ahmadi (2013) and Nalpanis, Hunt, & Barrett (1993)) and also it has been found that for a particle in saltation, when its height is above a few grain sizes ($z \gg d_p$), the most significant forces acting on it are drag and gravity (Nalpanis et al., 1993). Discrete phase modeling studies using ANSYS FLUENT (Landázuri et al., 2011) were performed over spherical particles 3–100 μm in diameter and with densities from 1000 to 2500 kg/m^3. The simulations considered different wind speeds. For example, it was observed that at a wind velocity of 0.5 m/s (same order of magnitude of the present study), the gravitational force is more important than drag force for particles greater than 6 μm, and fine particles were easily entrained by the wind and can be carried over long distances before settling. At higher speeds horizontal drag effects may become important.

Particles were injected 0.75 m upstream from the point of reference in the domain (sampler's central pore), with an initial free stream velocity of 0.4 m/s. There was no restriction for particles from hitting the surfaces outside the sampler prior to aspiration. The particle aspiration efficiency, *PAE*, of the sampler was calculated from (Anthony & Flynn, 2006):

$$PAE = \frac{A_C U_C}{A_S U_S} \quad (8)$$

where A_c is the critical area, defined as the area from which particles are aspirated into the sampler, as determined with particle release simulations; U_c is the free stream velocity within this critical area; A_s is the total area of the sampler pores and U_s is the velocity

through the sampler pores. The process consists on identifying the upper and lower limits of the area from where particles will be aspirated into the sampler. For the critical area calculation, 40 particles were injected along 1 cm vertical lines (*Z* direction) at a constant $X = -0.75$ m and at sequential lateral (*Y*) locations stepped through 0. mm increments. The release points must be unaffected by the torso and located below the height of the sampler. If the locations are changed, but still are not affected by the bluff body, and the release height for these particles is both upstream and above the height of the torso, then the same aspiration efficiency can be determined.

An important aspect to consider is that the farther away the point is, the larger the path, therefore, more time is required to track the particles and determine whether the particle got trapped or not in the sampler.

3.4. Grid adaption and manual scaling of grids for fluid flow evaluation

Both manual scaling and grid adaption were investigated. Manual scaling of grids was performed using the sampler 2 configuration, which is geometrically simpler. A scaling factor of 1.2 based on the number of nodes of each edge of the finer to coarser grid was chosen to ensure that the grids are different from each other.

The method of gradient adaption assumes that maximum error occurs in regions where large gradients of the flow variables (U_x, U_y, U_z, P, k and ε) exist. This strategy intends to equally distribute the error over the edges and minimizes the tendency of the initially coarse grid to be over-refined. Depending on how the coarse mesh was structured originally, edges with the highest errors could be refined, or those with the lowest errors could be coarsened in order to reduce the average error over the domain (Tam et al., 2000). In this study, the velocity in the *X* direction was chosen as field variable to minimize discretization errors during the adaption process. This was based on the fact that U_x is the main direction of the air flowing through the wind tunnel. In addition, this variable was more prone to show increases in its *GSE* as the simulation progressed than the rest. The approach used in this work multiplied the Hessian of the selected solution variable by the characteristic length scale, which is the cube root of the cell volume,

$$|e_i| = (V_{cell})^{\frac{1}{3}} \left| \frac{\partial^2 U_x}{\partial X_j^2} \right|_i \quad (9)$$

Introduction of the length scale helps to resolve both strong and weak disturbances, increasing the potential to get more accurate solutions (Fluent, Inc (2005) and Daunenhofer& Baron (1985)). In Eq. (9), the subscript *i* designates the group of elements sharing node *i*.

For the grid adaption process, the coarser grid was allowed to run until solution tolerances of 5.0×10^{-5} and 5.5×10^{-5} for samplers 1 and 2, respectively. It should be mentioned that the continuity equation was last to converge: when continuity had converged with a tolerance of 5.0×10^{-5} for sampler 1, the *GSE* for momentum, turbulent kinetic energy, and energy dissipation rate equations reached *GSE* in the order of 10^{-7}–10^{-9}. The grid was adapted by

setting the refinement criterion of a maximum U_x gradient to a threshold value that corresponded to a scaling factor of 1.4 between finer to coarser grids in terms of the total number of nodes in the whole domain. The original grid was not marked for coarsening and cells with gradient values above the refinement threshold criterion were refined. The scaling factor of 1.4 was used by Fluent® during the first adaption of the original grid, and it was preserved for the second adaption to get the third (finer) grid. This factor could have been chosen arbitrarily, as long as it is not too close to 1; the idea is that this ratio should represent grids that are sufficiently different from each other to be able to detect sensitivity to solution changes, but it should not be too large since more iterative steps would be necessary (Stern et al., 2001): computational effort should be minimized. An overall increase of 40% is considered appropriate for the analysis; once the grid we consider "coarser" converges, then, by changing the refinement by a percentage, will change the whole number of domain elements (changing their location), and the grids are no longer the same.

The new grid with adapted (split) cells was allowed to resolve the fluid flow field to the same *GSE* and the adaption procedure was repeated. Solutions from these three meshed domains were saved sequentially at global solution errors of 10^{-3}, 10^{-4} and lower, to evaluate iterative convergence and assess grid independence using the methods already described.

The details of scaled grids discussed in this work are presented in Table 1. Table 1a shows the grid density details of the *original (coarse)*, *moderate* and *fine* grids using sampler 2 (no filter included) and manual scaling. Table 1b presents the number of elements of both sampler configurations using grid adaption by gradient in U_X. The settings and boundary conditions for the models applied to the analyzed grids are presented in Table 2.

The case presented in Table 1 led to satisfactory results in terms of iterative convergence (Table 3a), but not for grid independence (Table 3b) and monotonic convergence (Table 3c). For this reason, manual scaling of the prototype that includes the filter and exhaust port (sampler 1) was not performed. In contrast, results from the verification process show iterative and monotonic convergence, as well as grid independence, when adapted grids are used, as shown in Table 4 and Table 5. The flow field solutions given by the first adapted grids at tolerances of 5.0×10^{-5} and 5.5×10^{-5} for samplers 1 and 2, respectively, were used for particle simulations. These solutions were also used to illustrate differences between configurations in locations other than the vicinity of the sampler. Moreover, a Gaussian model was fitted to the calculated *PAE* (Eq. (8)), reported in Table 6a. The statistical results from the regressions and the parameters that characterize the Gaussian models are presented in Table 6b.

4. Results and discussion

Manual generation of three successively scaled grids did not provide grid independence for all six degrees of freedom (Table 3b); only U_x, k and ε had R_2 values higher between 0 and 1. However, iterative convergence was reached for all degrees of freedom, since L_2 values are less than 5%, as shown in Table 3a. This suggested that more refined grids or less

tolerance was necessary. However, the flow field could not be solved at lower *GSE*, and further grid refinement could not be achieved due to memory limitations. The solution became divergent after a few iterations. This was corroborated by the low number of locations that showed monotonic convergence (Table 3c), especially for U_x, U_y and P at a *GSE* of 10^{-3}, and by the fact that their R_2 values were greater than 1, as shown in Table 3b.

The nature of the domain is complex since there are discretization cells with different sizes. It was clear that the grid density outside the sampler needed to be coarser than that inside the sampler, but even with more refinements there were some areas of the meshed domain, such as around the torso, that are still too coarse to be resolved to adequately describe the shape of the whole domain. To overcome this difficulty by manual refinement became impractical since the procedure became trial and error. A decrease in relaxation parameters provided improvements in terms of obtaining a converged solution in less time per iteration and even at lower tolerances. The simulations using sampler 1 required these adjustments. Relaxation parameter values agree with the recommended values for turbulent flow simulations (Barron & Salehi Neyshaburi, 2003).

Fig. 3 shows the regions of the domain that needed grid refinement, and provide a comparison between the original (coarse) and most refined grids (after second adaption). These are examples of locations that required more detail to adequately capture the geometric features of the physical domain; this is particularly evident in Fig. 3c and d where triangles were split (adapted) in the lateral parts of the torso.

The solutions from the three adaptive grids obtained were compared in terms of the L_2 error norms at three different *GSE*, the convergence ratios defining grid independence, and the percentage of locations that present monotonic convergence. As observed in Table 4, the simulations of the three adaptively-refined grids present relative L_2 error norms of less than 2.5% and 3.25%, for samplers 1 and 2, respectively, for each of the three *GSE* tolerances and the different degrees of freedom studied. Most of the relative error norms had values even less than 0.1%. Table 5a shows that all degrees of freedom evaluated at the different tolerances yield solutions that are grid independent; any of these simulations can be used as the proposed model to describe the samplers' efficiencies. In addition, the percentage of locations among the 1722 nodes evaluated with monotonic convergence is relatively high for degrees of freedom U_y, U_z, and to less extent, but still adequate, for P, k, ε and U_x (Table 5b).

As mentioned before, the critical aspiration area was defined on a specified plane (0.75 m upstream from the sampler) as the surface that contains the particles that will eventually enter the sampler. The planes were strategically picked so that from continuity the most particles released can be aspirated by the sampler, and also, upstream, the particles met the criteria of being out of the region affected by the presence of the bluff body, and downstream, the fluid flow became stabilized after it passes by the torso. Under these conditions a developed turbulent flow can be achieved and therefore a steady state study can be applied.

An illustration of critical areas for sampler 1 is presented in Fig. 4. The upward displacement of the critical aspiration area for larger particles reflects the effect of the gravitational force. Fig. 4c shows sample pathlines followed by particles contained in the critical areas as they approach the sampler. Calculated aspiration efficiencies are presented in Table 6. It is important to mention that the calculated aspiration efficiencies are the average values between the maximum and minimum aspiration efficiencies found, which only differ by less than 1.1%. As shown in Fig. 5, aspiration efficiencies for the two samplers are similar. From a particle perspective, the simplest configuration (sampler 2, no filter and no 4 mm exhaust port) can be used to characterize the flow field outside the sampler to calculate the efficiency. Fig. 5b presents the particle aspiration efficiency (*PAE*) curves along with a Gaussian fit for each case. These horizontally oriented samplers overestimate the efficiency, which is consistent with previous studies (Anthony et al., 2010) as well as with wind tunnel data using the conventional closed-face 37-mm cassette (Li et al., 2000). It was observed that the 0° down orientation samplers overestimate the aspiration efficiencies whereas the 30° oriented sampler compares better to mannequin wind tunnel experiments. Also, the sampler configurations, object of this verification study was designed to be positioned on the torso of a worker and it would be uncommon that the sampler remains horizontally fixed all the time as the tubing connecting the sampler to the sample pump typically interferes with such a positioning (Anthony et al., 2010). Nonetheless, the verification procedures and comparison between two construction methods (through manual and grid adaption), can be applied to any type of CFD simulation.

Table 6 also presents the statistical results for each approximation and the respective equations to model *PAE* when a horizontally oriented sampler is used. It is interesting to point out that the curves from Fig. 5b consist mainly of three regions, as defined previously for other configurations (Chung & Dunn-Rankin, 1992): the first region is defined as the asymptotic region due to the fact that aspiration efficiency of small particles approaches 100%; the second region, called the overshoot region, corresponds to *PAE* greater than 100%, which is a consequence of the fact that particles with small inertia deviate from the fluid streamlines and are aspirated; the third region is the decline region, where efficiency drops presumably because large particles with relatively large settling velocities are not suctioned by the sampler.

5. Conclusion

CFD was used to perform fluid flow evaluation studies and calculate the particle aspiration efficiency of two horizontally facing-the-wind occupational air samplers. The samplers are based on a commonly used 37-mm cassette with a new porous inlet design and mainly differ on the outlet design. The Standard k–ε turbulent model was applied to solve the turbulent Navier Stokes equations. Second order discretization schemes, along with the Gauss Cell based method for determination of gradients and derivatives were used. Iterative convergence and grid independence using three scaled grids were verified on manually and adaptively scaled grids by means of grid adaption by gradient of U_x. Grid adaption proved to be a better scaling tool than manual scaling since it guaranteed grid independence throughout the domain where particle trajectory simulations were performed to calculate the sampler aspiration efficiency, and also minimized simulation time. It is strongly suggested

to use grid adaption techniques for problems where different scales are present in the domain. From a particle perspective, the sampler without filter and exhaust port can be used to characterize the flow field outside the sampler to calculate the efficiency; allowing for geometrical simplifications during mesh generation.

Acknowledgments

This project was funded by the U.S. National Institute for Occupational Safety and Health (R21OH009114). The content is solely the responsibility of the authors and does not necessarily represent the official views of the U.S. National Institute of Occupational Safety and Health. The authors would also like to thank Universidad San Francisco de Quito, through the College of Science and Engineering, for supporting CFD research work.

References

Anagnostopoulos P, Iliadis G. Numerical study of the blockage effects on viscous flow past a circular cylinder. International Journal for Numerical Methods in Fluids. 1996; 22:1061–1074.

Anderson KR, Anthony TR. Uncertainty in aspiration efficiency estimates from torso simplifications in computational fluid dynamics simulations. Annals of Occupational Hygiene. 2013; 57(2):184–199. [PubMed: 23006817]

Anthony TR, Flynn MR. Computational fluid dynamics investigation of particle inhalability. Journal of Aerosol Science. 2006; 37:750–765.

Anthony TR, Landázuri TC, Van Dyke M, Volckens J. Design and computational fluid dynamic investigation of a personal, high-flow, inhalable sampler. Annals of Occupational Hygiene. 2010; 54:427–442. [PubMed: 20418278]

Barron RM, Salehi Neyshaburi AA. Effects of under-relaxation factor on turbulent flow simulations. International Journal of Numerical Methods in Fluids. 2003; 42:923–928.

Bird AJ. Use of numerical calculations to simulate the sampling efficiency performance of a personal aerosol sampler. Aerosol Science and Technology. 2005; 39:596–610.

Chung IP, Dunn-Rankin D. Numerical simulation of two-dimensional blunt body sampling in viscous flow. Journal of Aerosol Science. 1992; 23:217–232.

Daunenhofer JF, Baron JR. Grid Adaption for the 2D Euler Equations. American Institute of Aeronautics and Astronautics. 1985

Dussin D, Fossati M, Guardone A, Vigevano L. Hybrid grid generation for two-dimensional high-Reynolds flows. Computers Fluids. 2009; 38:1863–1875.

Fluent Inc. Fluent User's Guide. 2005

Griffiths WD, Boysan F. Computational Fluid Dynamics (CFD) and empirical modeling of the performance of a number of cyclone samplers. Journal of Aerosol Science. 1996; 27:281–304.

Landázuri, AC.; Brauneis, J.; Sáez, AE.; Betterton, EA. 2011 AIChE Annual Meeting Proceedings Environmental Division. 2011. Discrete Phase Modeling of Atmospheric Particulate Transport from Mine Tailings.

Li S, Lundgren DA, Rovel-Rixx D. Evaluation of Six Inhalable Aerosol Samplers. American Industrial Hygiene Association Journal. 2000; 61:506–516. [PubMed: 10976680]

Morsi SA, Alexander AJ. An investigation of particle trajectories in two-phase flow systems. Journal of Fluid Mechanics. 1972; 55:193–208.

Nalpanis P, Hunt JCR, Barrett CF. Saltating particles over flat beds. Journal of Fluid Mechanics. 1993; 251:661–685.

Richmond-Bryant J. Verification testing in computational fluid dynamics: an example using Reynolds-averaged Navier-Stokes methods for two-dimensional flow in the near wake of a circular cylinder. International Journal for Numerical Methods in Fluids. 2003; 43:1371–1389.

Roache, PJ. Verification and Validation in Computational Science and Engineering. Hermosa Publishers; Albuquerque, NM: 1998.

Stern F, Wilson RV, Coleman HW, Paterson EG. Comprehensive approach to verification and validation of CFD simulations—Part 1: methodology procedures. Journal of Fluids Engineering. 2001; 123:793–802.

Tam A, Ait-Ali-Yahia D, Robichaud MP, Moore M, Kozel V, Habashi WG. Anisotropic mesh adaptation for 3D flows on structured and unstructured grids. Computational Methods in Applied Mechanics and Engineering. 2000; 189:1205–1230.

Tu, J.; Inthavong, K.; Ahmadi, G. Chapter 6: Fundamentals of Particle Dynamic. Springer; New York: 2013. Computational Fluid and Particle Dynamics in the Human Respiratory System Biological and Medical Physics, Biomedical Engineering.

Zdravkovich, MM. Flow Around Circular Cylinders: Applications. University Press; New York: 2003.

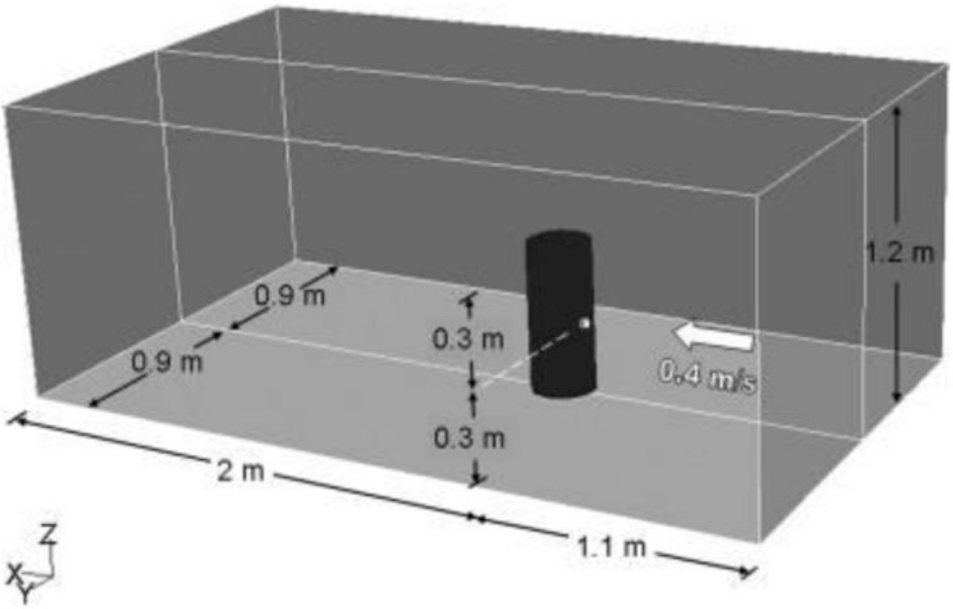

Fig. 1.
Wind tunnel and torso geometry, showing relative location of the sampler.

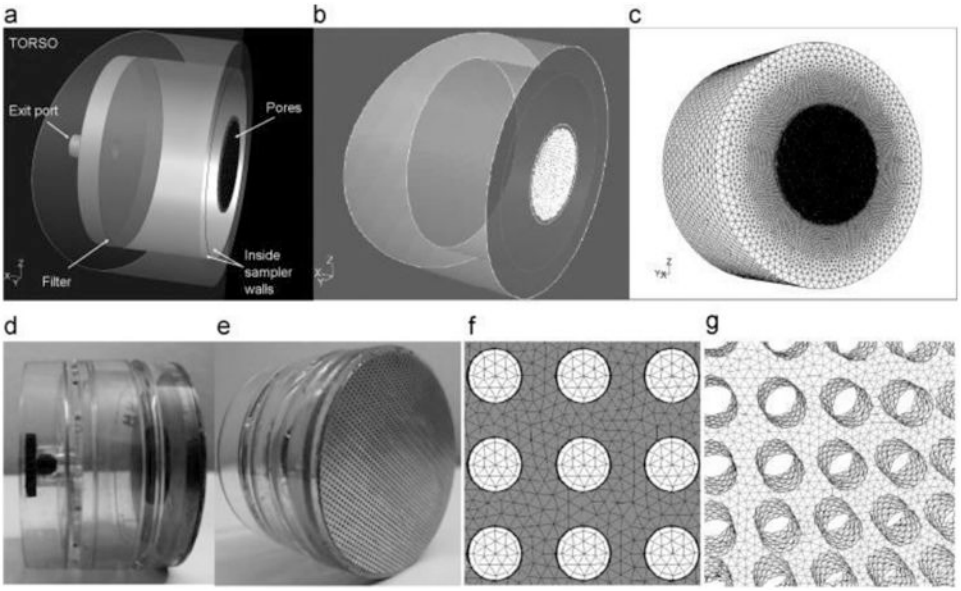

Fig. 2.

Geometrical representation of the sampler prototypes. (a) Sampler 1 configuration, (b) sampler 2, where filter and exhaust port are excluded, (c) grid detail in the outer walls of the sampler, (d) and (e) two views of actual sampler 1 prototype, (f) and (g) two perspectives of the sampler pore openings showing grid details.

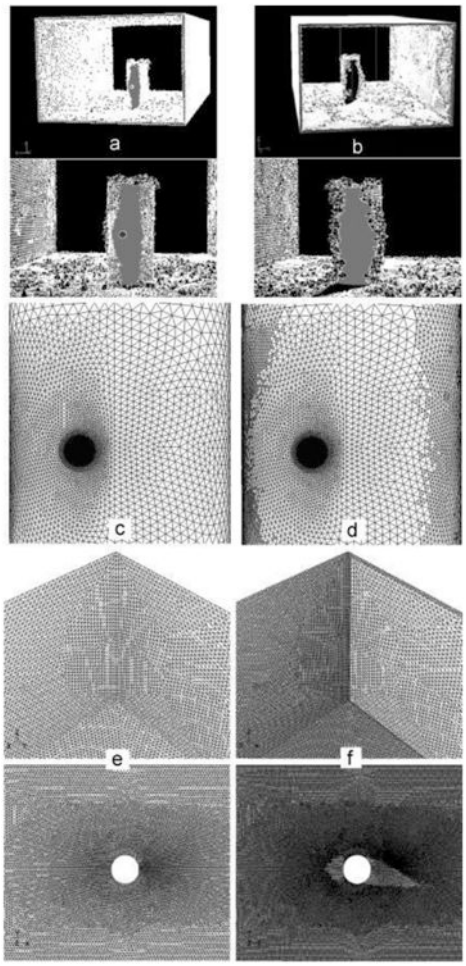

Fig. 3.

Different views of adaption markings inside wind tunnel and around torso. (a) Front view, looking toward torso and sampler, (b) back view, (c) original torso outer face grids showing sampler location, (d) torso outer face after second adaption (grid name: original_2_ad2); (e) and (f) comparison of original (left) and adapted (right) wind tunnel corner and bottom wall grids.

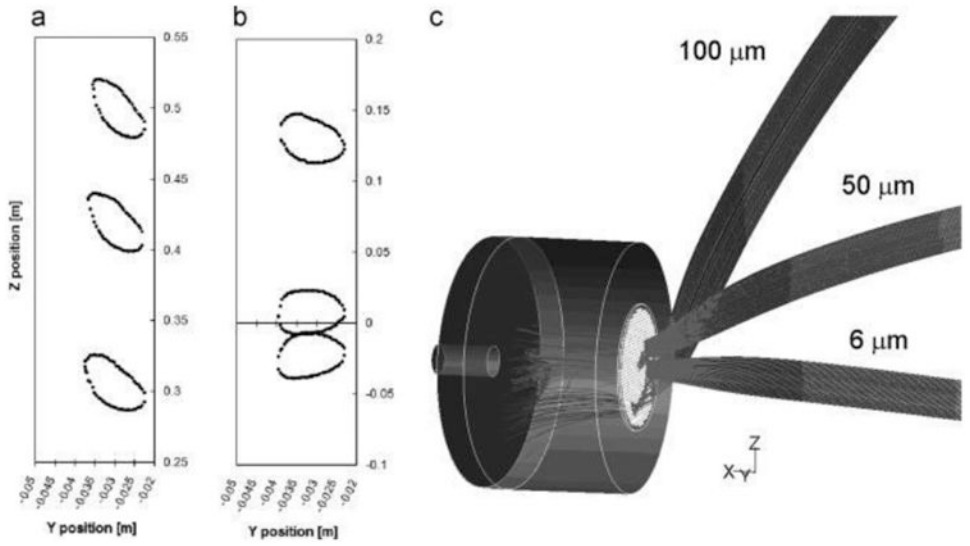

Fig. 4.

Aspiration critical areas for the sampler with filter and exhaust port (sampler 1). Particles are released 0.75 m away from the central pore of the samplers. Particle sizes are (from top-to-bottom: (a) 100, 75, 50, (b) 25, 12.5 and 6 μm. Note that location of critical area lowers as particle size decreases due to gravitational effects. (c) Traces of spherical particles of specified diameter that are suctioned by the sampler. Only particles with trajectories that end in the vicinity of the sampler are shown. Particles were released from positions X=−0.75 m, Y =0.315 that extended through 10 mm lines in the Z direction beginning at Z=0.5 (100 μm), 0.3 (50 μm) and −0.025 (6 μm).

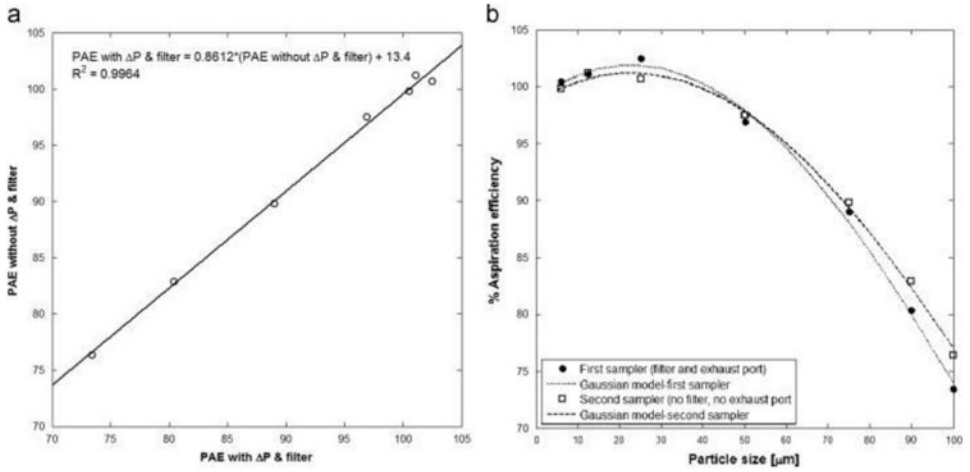

Fig. 5.

(a) Comparison of both horizontally oriented samplers based on the percentage of aspiration efficiency. (b) Aspiration efficiency curves obtained from particle simulations.

Table 1

(a) Grid details for grids used in sampler 2 simulations using manual scaling; (b) number of finite elements for both sampler configurations using grid adaption.

(a) Sampler 2 grid details using manual scaling

Entity name	Name of simulation grids		
	original_2	*moderate_2*	*fine_2*
	No. of elements		
Volume[a]			
Nearsam	715,597	1,096,885	1,514,221
Air1	730,280	1,118,420	1,534,274
Fluid+Y	1,160,693	2,247,261	2,049,969
Fluid-Y	950,920	1,898,118	2,023,192
Edge			
Nodes around each 254-μm pore perimeter	12	15	18
Grid Info			
Cell	4,266,148	6,299,870	9,105,903
Faces	8,761,244	12,932,134	18,666,982
Nodes	824,679	1,214,402	1,744,001

(b) Number of finite elements for both sampler configurations using grid adaption

	Name of simulation grids – sampler 1		
Element type	*original_1*	*original_1_ad1*	*original_1_ad2*
Cells	4,424,545	5,814,010	6,842,338
Faces	9,084,823	12,082,138	14,644,267
Nodes	854,607	1,196,411	1,680,471
	Name of simulation grids – sampler 2		
Element type	*original_2*	*original_2_ad1*	*original_2_ad2*
Cells	4,266,148	5,548,772	6,415,470
Faces	8,761,244	11,524,468	13,698,981
Nodes	824,679	1,138,158	1,563,506

[a]Representative air volumes. Nearsam represents the volume of air right outside the inlet pores, Air1 is the volume inside the cassette, Fluid $+Y/-Y$ are the volumes of air in the $+Y/-Y$ directions of the wind tunnel.

Table 2

Boundary conditions and characteristics of 2nd order upwind k–ε model for sampler 1.

Sampler 1 (Filter and 4-mm exhaust port included)		
Boundary name	**Boundary type**	**Boundary condition**
wtin	Velocity inlet	
		Wind tunnel inlet velocity: 0.4 m/s
		Turbulent intensity: 8%
		Turbulent viscosity ratio: 10
exitfac	Velocity inlet	
		Suction velocity through port: −13.263 m/s
		Turbulent intensity: 8%
		Turbulent viscosity ratio: 215
finface	Porous jump	
		Permeability: m^2
		Filter thickness: m
Under relaxation parameters:		
Pressure: 0.2, density: 1, body forces: 1, momentum: 0.5, k: 0.5, ε: 0.5		
Sampler 2		
Boundary name	*Boundary type*	*Boundary condition*
wtin	Velocity inlet	
		Wind tunnel inlet velocity: 0.4 m/s
		Turbulent intensity: 8%
		Turbulent viscosity ratio: 10
finface	Velocity inlet	
		Suction velocity through opening: −0.1972 m/s
		Turbulent intensity: 8%
		Turbulent viscosity ratio: 10
Under relaxation parameters (default)		
Pressure: 0.3, density: 1, body forces: 1, momentum: 0.7, k: 0.8, ε: 0.8		

Table 3

(a) Relative % L_2 error norm investigating non-linear convergence when manual scaling is used: 1722 nodes upstream of sampler 2 were used in the calculations, (b) three-mesh convergence ratio, R_2, over 1722 nodes upstream of sampler 2 for manual mesh scaling and (c) and percent of locations that show monotonic convergence. This is an example of unsatisfactory results when manual scaling is used.

Grid name		**(a) Relative % L_2 error norm**					
	GSE	U_x	U_y	U_z	P	k	ε
original_2	10^{-3}–10^{-4}	0.0573	1.1978	0.7238	0.5804	0.0153	0.0148
	10^{-4}-5.5×10^{-5}	0.0028	0.0921	0.0214	0.0305	0.0014	0.0014
moderate_2	10^{-3}–10^{-4}	0.0611	0.6538	0.7262	0.5527	0.0171	0.0148
	10^{-4}–5.5×10^{-5}	0.0459	0.0649	0.0413	0.0389	0.0020	0.0018
fine_2	10^{-3}–10^{-4}	0.1411	0.7152	2.3124	1.2312	0.0292	0.0270
	10^{-4}–5.5×10^{-5}	0.0050	0.0608	0.0478	0.0435	0.0018	0.0015
	(b) Three-mesh convergence ratio						
	GSE	U_x	U_y	U_z	P	k	ε
	10^{-3}	2.1774	2.0361	0.5161	1.6161	0.1393	0.4626
	10^{-4}	1.8805	2.2401	0.6348	1.4102	0.1395	0.4625
	5.5×10^{-5}	1.8739	2.2829	0.6401	1.4126	0.1396	0.4627
	(c) Percent of locations that show monotonic convergence						
	GSE	U_x	U_y	U_z	P	k	ε
	10^{-3}	11.8	2.9	83.6	23.5	99.7	99.7
	10^{-4}	58.2	100.0	99.9	71.7	62.7	58.4
	5.5×10^{-5}	55.6	100.0	99.9	70.3	62.3	57.8

Table 4

Relative % L_2 error norm investigating non-linear convergence when grid adaption is used: 1722 nodes upstream of the samplers were used in the calculations.

Grid name	*GSE*	U_x	U_y	U_z	P	k	ε
				Sampler 1			
original_1	10^{-3}–10^{-4}	0.0361	1.0547	0.2675	0.4795	0.0086	0.0095
	10^{-4}–5×10^{-5}	0.0033	0.1101	0.0348	0.0327	0.0012	0.0012
original_1_ad1	10^{-3}–10^{-4}	0.1510	1.5093	2.4235	1.3012	0.0296	0.0262
	10^{-4}–5×10^{-5}	0.0167	0.0789	0.2024	0.1411	0.0031	0.0026
original_1_ad2	10^{-3}–10^{-4}	0.2175	1.2307	1.7590	1.2302	0.0731	0.1171
	10^{-4}–5×10^{-5}	0.0030	0.0275	0.0144	0.0274	0.0004	0.0004
		Sampler 2					
original_2	10^{-3}–10^{-4}	0.0573	1.1978	0.7238	0.5804	0.0153	0.0148
	10^{-4}–5.5×10^{-5}	0.0028	0.0921	0.0214	0.0305	0.0014	0.0014
original_2_ad1	10^{-3}–10^{-4}	0.1385	1.5287	3.2356	1.1693	0.0275	0.0268
	10^{-4}–5.5×10^{-5}	0.0100	0.0416	0.1090	0.0855	0.0019	0.0016
original_2_ad2	10^{-3}–10^{-4}	0.1988	1.3824	1.2636	0.9729	0.0711	0.1170
	10^{-4}–5.5×10^{-5}	0.0042	0.0308	0.0360	0.0395	0.0006	0.0006

Table 5

Three-mesh convergence ratio, R_2, over 1722 nodes upstream of the sampler, and percent of locations that show monotonic convergence when grid adaption is used.

Three-mesh convergence ratio, R_2						
	U_x	U_y	U_z	P	k	ε
GSE	**Sampler 1**					
$\mathbf{10^{-3}}$	0.4419	0.3493	0.2303	0.3645	0.4425	0.4882
$\mathbf{10^{-4}}$	0.8996	0.2074	0.0883	0.5695	0.6282	0.8579
$\mathbf{5\times10^{-5}}$	0.9230	0.1990	0.0937	0.5857	0.6184	0.8581
	Sampler 2					
$\mathbf{10^{-3}}$	0.4081	0.2624	0.2521	0.2973	0.4147	0.4703
$\mathbf{10^{-4}}$	0.6961	0.1808	0.0561	0.3835	0.6176	0.8242
$\mathbf{5.5\times10^{-5}}$	0.7045	0.1783	0.0538	0.3872	0.6135	0.8249
Percent of locations that show monotonic convergence						
	U_x	U_y	U_z	P	k	ε
GSE	Sampler 1					
$\mathbf{10^{-3}}$	83.3	100.0	98.4	83.0	89.8	89.8
$\mathbf{10^{-4}}$	37.6	100.0	98.5	57.7	60.9	55.3
$\mathbf{5\times10^{-5}}$	32.9	100.0	98.5	55.1	60.0	53.0
	Sampler 2					
$\mathbf{10^{-3}}$	84.4	100.0	98.4	83.2	89.9	89.9
$\mathbf{10^{-4}}$	58.2	100.0	99.9	71.7	62.7	58.4
$\mathbf{5.5\times10^{-5}}$	55.6	100.0	99.9	70.3	62.3	57.8

Table 6

(a) Aspiration efficiencies for both samplers and (b) Gaussian fits of *PAE*s for both samplers.

(a) % Aspiration efficiency

Particle size, d_p [μm]	Sampler 1 (filter and exhaust port included)	Sampler 2 (no filter, no exhaust port)
6.0	100.5	99.8
12.5	101.1	101.2
25.0	102.5	100.7
50.0	96.9	97.5
75.0	89.0	89.8
90.0	80.4	82.9
100.0	73.4	76.4

(b) % Aspiration Efficiency = a exp[−(d$_p$−b)^2/c]

	Sampler 1			Sampler 2		
Coefficient	**Value**	**95% confidence bounds**		**Value**	**95% confidence bounds**	
a	101.9	100.7	103.2	101.2	100.3	102.1
b	22.84	15.75	29.94	22.85	16.83	28.86
c	136.4	120.3	152.5	147.8	133.1	162.5

Sampler	SSE	R^2	RMSE	Adjusted R^2
1	2.9936	0.9962	0.9942	0.8651
2	1.5683	0.9973	0.9959	0.6262